An Investigation of Ionospheric TEC Prediction Maps Over China Using Bidirectional Long Short-Term Memory Method

Shuangshuang Shi[1,2] , **Kefei Zhang**[1,2,3], **Suqin Wu**[1,2] , **Jiaqi Shi**[1,2], **Andong Hu**[4], **Huajing Wu**[1,2], and **Yu Li**[5]

[1]Jiangsu Key Laboratory of Resources and Environmental Information Engineering, China University of Mining and Technology, Xuzhou, China, [2]School of Environmental Science and Spatial Informatics, China University of Mining and Technology, Xuzhou, China, [3]Satellite Positioning for Atmosphere, Climate and Environment (SPACE) Research Centre, RMIT University, Melbourne, VIC, Australia, [4]CIRES, University of Colorado, Boulder, CO, USA, [5]China Earthquake Networks Center, China Earthquake Administration, Beijing, China

Abstract The ionospheric total electron content (TEC) is an important ionospheric parameter, and it is widely utilized in research such as space weather prediction and precise positioning. However, it is still challenging to develop an ionospheric TEC prediction model with high accuracy. In this study, a new ionospheric TEC model over China was developed using the bidirectional long short-term memory (bi-LSTM) method and observations from 257 ground-based global navigation satellite system (GNSS) stations in the Crustal Movement Observation Network of China from January 2018 to December 2021. The root mean square errors of the bi-LSTM-based model's 1 and 2 hr ahead predictions on the test data set (from June 2021 to December 2021) are 1.12 and 1.68 TECU, respectively, which are 75/50/32% and 72/48/22% smaller than those of the IRI-2016, artificial neural network and LSTM-based models, correspondingly. The bi-LSTM-based model shows the best performance, which is most likely due to the fact that the sequence information in both forward and backward directions is taken into consideration in the new model. In addition, the diurnal variation, seasonal variation of the ionospheric TEC, and variations under geomagnetic storm conditions are successfully captured by the bi-LSTM-based model. Moreover, the TEC maps resulting from the bi-LSTM model agree well with those obtained from the final ionospheric product from the Chinese Academy of Sciences. Hence, the new model can be a good choice for the investigation of the spatiotemporal variation trend in the ionosphere and GNSS navigation.

Plain Language Summary The ionospheric total electron content (TEC) is the total number of free electrons along a signal propagation path in a cross section of one square meter, and the ionospheric delay error of the signal from the global navigation satellite system (GNSS) is proportional to the value of TEC. The variation of the ionospheric TEC can also be used to study the variations in space weather. In this study, a new ionospheric TEC model over China based on the bidirectional long short-term memory (bi-LSTM) method and long-term ground-based observations at 257 GNSS stations from the Crustal Movement Observation Network of China was developed and subsequently validated. The main reason for the selection of the bi-LSTM model is for its consideration of the sequence information in both forward and backward directions. The prediction results of the new model show that in comparison with that of three other models, including the artificial neural network, LSTM, and traditional IRI-2016 models, the new model is the best performer. Furthermore, the bi-LSTM model also successfully captures the diurnal and seasonal variations of the ionospheric TEC and the TEC variations under geomagnetic storm conditions.

1. Introduction

The ionosphere is the ionized part of Earth's upper atmosphere with an altitude of about 60–1,000 km, which plays an important role in the transionospheric radiopropagation applications and is closely related to human activities (Klobuchar, 1987). When a signal from the global navigation satellite system (GNSS) is propagated through the ionosphere, it encounters many effects, such as dispersion, refraction, and group delay. The magnitude of these effects is proportional to the total electron content (TEC) along the signal propagation path. In addition, the TEC value can also reveal the activity of either the solar wind or the geomagnetic field (Cherniak & Zakharenkova, 2018; Ngwira et al., 2012; Thomas et al., 2017). Therefore, predicting the ionospheric TEC

with high accuracy is important in transionospheric radiopropagation-related applications and in space weather prediction.

There are mainly two types of models for predicting the ionospheric TEC, that is, physics-based and empirical models. The physics-based models are based on mathematical representations of physical laws to depict ionospheric parameters, for example, the Coupled Thermosphere Ionosphere Plasmasphere Electrodynamics Model (CTIPe) (Fuller-Rowell & Rees, 1980), the Time Dependent Ionospheric Model (TDIM) (Sojka, 1989), the Sheffield University Plasmasphere Ionosphere Model (SUPIM) (Bailey et al., 1997), and the Global Core Plasma Model (GCPM) (Gallagher et al., 2000). These models are complex and often used to investigate the physical and chemical processes of the upper atmosphere. However, their accuracy is highly affected by the quality of input data and negligence of some physical processes. The empirical models are based on mathematical fittings to historic experimental data from ground-based ionosondes, incoherent scatter radars, topside sounders, and satellites. Typical empirical models include the Bent model (Bent et al., 1972), the Klobuchar model (Klobuchar, 1987; Wang et al., 2016), the NeQuick model (Giovanni & Radicella, 1990; Nava et al., 2008), the International Reference Ionosphere (IRI) model (Bilitza, 1990, 2018; Bilitza et al., 2017), and the global Neustrelitz TEC Model (NTCM) (Jakowski et al., 2011). These empirical models are computationally fast and easy to be applied to ionospheric prediction. However, in their standard way of operation, these models reflect the "climate" and regular variations in the ionospheric TEC well, while the perturbations and irregularities cannot be reflected. In addition to the above-mentioned empirical models, there are other empirical models that predict the ionospheric TEC based on TEC time series, for example, the Standard Persistence Model (SPM) (García-Rigo et al., 2011), the 27-day median model (MediMod) (Rich et al., 2003), the auto-regressive moving average (ARMA) model (Krankowski et al., 2005), the Fourier Series Expansion model (Badeke et al., 2018), and the Holt-Winter model (Elmunim et al., 2017). However, these time series dependent models do not consider the trend in the parameters (e.g., the solar and geomagnetic activity parameters) that affect the ionospheric variations, which make it difficult for these models to be used to predict the fluctuations of the ionospheric TEC.

For predicting the ionospheric TEC under disturbed space weather and for acquiring high-accuracy ionospheric TEC for satellite navigation, a new ionospheric TEC model using a new approach needs to be investigated, and the following two factors need to be considered: (a) The rapid growth in the number and quality of the observations and the continuous increase in computational power and (b) the sun and geomagnetic factors, which lead to high variability in the ionospheric TEC. For these two aspects, deep learning methods are promising as they are well known for progressively extracting higher-level features from the raw input variables, and one of the benefits is that there is no need to identify or specify the functional relationship (e.g., linear or nonlinear) of the model. This is why deep learning methods are often used to model the ionospheric TEC (Li, Zhao, et al., 2021; Ruwali et al., 2021; Xiong et al., 2021; Zewdie et al., 2021; Zhukov et al., 2020).

Deep learning methods have been widely used in the prediction of the ionospheric TEC for a single station (Huang et al., 2015; Kaselimi et al., 2020; Ruwali et al., 2021; Srivani et al., 2019; Xiong et al., 2021; Zewdie et al., 2021), for a region (Li et al., 2020; Okoh et al., 2016, 2019, 2020; Razin et al., 2015; Sabzehee et al., 2018; Song et al., 2018; Tebabal et al., 2019; Uwamahoro et al., 2018), and for the globe (Cesaroni et al., 2020; Chen et al., 2019; Liu et al., 2020; Zhukov et al., 2020). TEC prediction models for a single station based on the artificial neural network (ANN) method (Huang et al., 2015; Huang & Yuan, 2014), the long short-term memory (LSTM) method (Kaselimi et al., 2020; Srivani et al., 2019; Xiong et al., 2021; Zewdie et al., 2021), and the hybrid deep learning method (Ruwali et al., 2021), all have recently shown promising results. Both the LSTM and hybrid deep learning methods have shown better performance than the ANN method. In addition, the accuracy of these single station models was dependent on the geographical location of the station and solar and geomagnetic activity levels. To meet the requirement for regional applications, some scholars developed regional models using the ANN method and measurements from ground-based and space-borne GNSS. However, the ANN algorithm failed to capture the long-term dependence in these data sets and with the increase of the number for hidden layers, the complexity increased and the convergence rate slowed down. Besides, due to the fact that the global prediction models were primarily based on machine learning techniques and global ionospheric maps (GIMs), the equatorial anomaly could hardly be captured by these global models (Orus Perez, 2019).

The Crustal Movement Observation Network of China (CMONOC) is a fundamental facility consisting of about 260 continuous GNSS stations and has been widely used to monitor plate tectonics earthquakes, wide-area differential global positioning system (GPS), and meteorology. The network provides a large number of observations
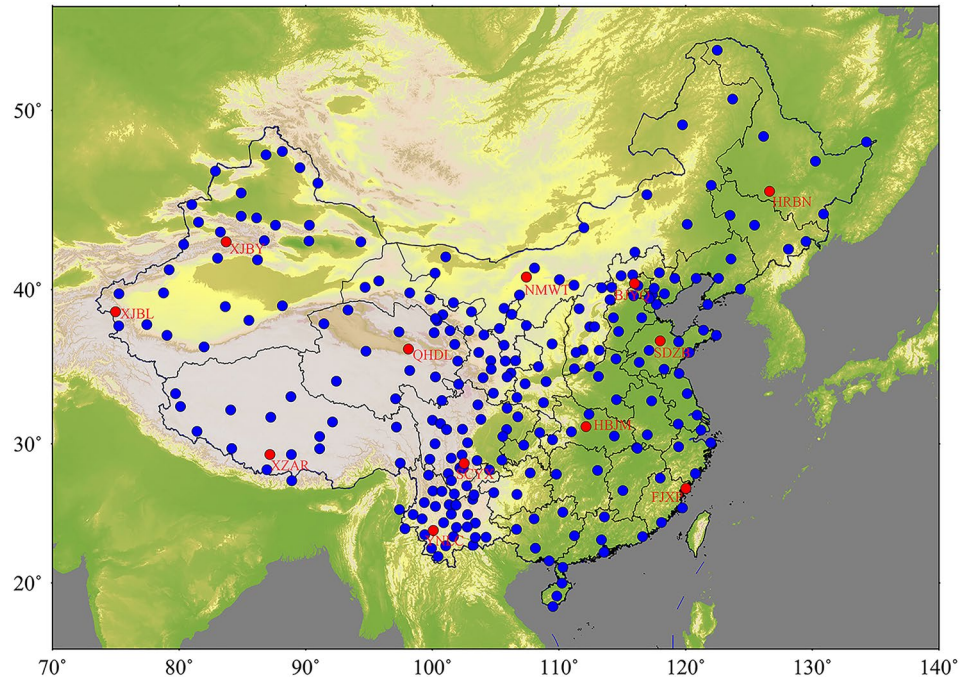
Figure 1. Spatial distribution of the 257 global navigation satellite system (GNSS) stations from the Crustal Movement Observation Network of China (CMONOC). The stations marked with blue and red dots were used to develop and test the new model, respectively. GNSS, global navigation satellite system and CMONOC, Crustal Movement Observation Network of China.

with high accuracy, high stability, and rapid real-time data. However, limited research has been conducted so far based on measurements from the CMONOC and deep learning methods to establish models for predicting the ionospheric TEC at single stations (Xiong et al., 2021). Thus, it is beneficial to use these abundant ground-based GPS observations and advanced deep learning methods to predict the ionospheric TEC over China. In this study, a new ionospheric TEC model was developed over China using these ground-based GPS observations and the bidirectional Long Short-Term Memory (bi-LSTM) method. Compared with the ANN and LSTM methods, the bi-LSTM method uses two independent recurrent neural networks (RNNs) to allow the network to take into consideration both backward and forward information in sequence. Moreover, the ANN, LSTM, and International Reference Ionosphere (IRI-2016) models were all tested for the comparison of their performance.

The organization of the paper is as follows. The data sets used and the variable set selected for modeling are introduced in Section 2. The ANN, LSTM, and bi-LSTM methods are described in Section 3. The validations of the bi-LSTM model and comparison with other models for geomagnetic quiet and storm conditions are presented in Section 4. Discussion and conclusion are given in Section 5.

2. Data

2.1. Ground-Based GPS Data

The ground-based GPS data include measurements at 257 permanent GNSS stations from the CMONOC that were used in this study, and the geographic locations of these stations are shown in Figure 1, where the GNSS stations that are marked with blue (245) and red (12) dots were used to develop and test the new model, respectively. The coordinates of the 12 test stations are listed in Table 1.

The absolute slant TEC (STEC) of a GPS signal is the total number of free electrons along the path of the GPS signal in a cross section of one square meter (unit: TECU, 1 TECU = 10^{16} el/m²), which can be obtained from simultaneous dual-frequency measurements collected at the ground-based GNSS station (Mannucci et al., 1998):

$$\text{STEC} = \frac{f_1^2 f_2^2}{40.28 \left(f_1^2 - f_2^2 \right)} \left(P_2 - P_1 + \Delta b_k + \Delta b^s \right) \tag{1}$$

Table 1
List of Selected CMONOC Stations for Test

Station code	Geographic latitude (°N)	Geographic longitude (°E)	Geomagnetic latitude (°N)
Geographic latitude: 20°N~30°N			
XZAR	29.27	87.18	20.28
SCYX	28.65	102.51	19.16
FJXP	26.88	120.02	17.58
YNLC	23.87	100.08	14.44
Geographic latitude: 30°N~40°N			
XJBL	38.65	74.97	30.41
SDZB	36.81	117.99	27.41
QHDL	36.30	98.10	26.87
HBJM	31.17	112.12	21.67
Geographic latitude: 40°N~50°N			
HRBN	45.70	126.62	36.60
XJBY	42.83	83.72	33.97
NMWT	40.75	107.42	31.20
BJYQ	40.37	115.97	30.91

Note. CMONOC, Crustal Movement Observation Network of China.

where P_1 and P_2 are the simultaneous pseudorange measurements on the two frequencies f_1 and f_2, respectively; Δb_k and Δb^s are the differential code biases (DCBs) of the receiver and satellite, respectively. The ionospheric TEC and DCBs can be estimated by the least-squares method (Chen et al., 2017; Li et al., 2012).

The ionosphere is usually modeled as a single-layer model (SLM), which assumes that all electrons are concentrated on a thin shell (Schaer, 1999). The STEC can be projected to the vertical total electron content (VTEC) at the ionospheric pierce point (IPP), the intersection of the signal path and the thin shell, using a mapping function under the assumption of spherical symmetry:

$$VTEC = STEC/M(e) \tag{2}$$

where $M(e)$ is the mapping function, and

$$M(e) = \left[1 - \left(\frac{R\cos(e)}{R+h} \right)^2 \right]^{-1/2} \tag{3}$$

In Equation 3, e is the elevation angle; R and h are the effective mean Earth radius and height of the IPP, respectively.

The observations from the CMONOC have a temporal interval of 30 s and a cutoff elevation angle of 15°. Finally, a total of 776,132,612 data points of the ionospheric VTEC with a 30 s time resolution were obtained. The ionospheric VTEC data were averaged over 1 hr intervals for smoothing out spikes and reducing the volume of the data. After this procedure was performed, the number of hourly VTEC values was 6,456,449.

2.2. Variables

The solar radio flux at a wavelength of 10.7 cm (F10.7) and Dst indices were used as the solar and geomagnetic activity variables, respectively. Day of year (DOY), hour of day (HOD), local time (LT), and geographic longitude and latitude were used as the variables of the deep learning models to be developed to describe the variations of the ionospheric TEC over time and space. These variables are independent and form the variable vector. In the development of the bi-LSTM model, the variable vectors of the previous 24 hr at the same station were treated as an independent variable set, and the VTECs in the next 2 hours (i.e., the 25th and 26th) were considered to be dependent on the variable set.

3. Methods

Neural networks, which mimic networks of biological neurons, are inspired by the human brain. They are widely used in many fields, such as classification, pattern recognition, linear and nonlinear data fitting, and time series forecasting (Li, He, et al., 2021; Okoh et al., 2019, 2020; Tulasi Ram et al., 2018). In this study, a three-layer neural network was used to create a multivariate regression model for predicting the ionospheric TEC. For a numerical continuous trend of the input data for the ANN model, the DOY and HOD in the input layer were respectively decomposed into two quadrature components (Williscroft & Poole, 1996):

$$\begin{cases} DOY_s = \sin\left(\frac{2\pi \times DOY}{365.25} \right) \\ DOY_c = \cos\left(\frac{2\pi \times DOY}{365.25} \right) \end{cases} \tag{4}$$

$$\begin{cases} HOD_s = \sin\left(\frac{2\pi \times HOD}{24} \right) \\ HOD_c = \cos\left(\frac{2\pi \times HOD}{24} \right) \end{cases} \tag{5}$$

where the subscripts s and c stand for the sine and cosine components, respectively.

The back-propagation learning algorithm and mini-batch gradient descent method (Ruder, 2016) were used to train the ANN model. The tansig function was used as the activation function between the input and hidden layers and also as the activation function between the hidden and output layers. The root mean squared error (RMSE) was used as the loss function. Observations of the stations marked with blue dots in Figure 1 from 1 January 2018 to 31 December 2020 (from 1 January 2021 to 31 May 2021) were used as the training (validation) data set. A total of eight input layer neurons (DOY$_s$, DOY$_c$, HOD$_s$, HOD$_c$, GLon, GLat, F10.7, and Dst) and two output layer neurons (VTECs in the next 2 hr) were used to develop the ANN model. Moreover, one hidden layer was used because we found that including more than one hidden layer could not significantly improve the ANN model's accuracy. And the use of multiple hidden layers was more prone to lead to bad local minima results. Finally, our training results indicate that when the number of neurons in the hidden layer is 43, the optimization criterion (RMSE) has the minimum value of 1.87 TECU.

Unlike the ANN method, the recurrent neural network (RNN) was designed to better process time sequence information. It takes into consideration the sequential variation among the sample data and has been widely used in the process of short-term sequences (Kaselimi et al., 2020; Liu et al., 2020; Srivani et al., 2019). The LSTM method, a commonly used gated RNN, can pass relevant information down the long chain of sequences to make predictions. It was developed to solve the problem of short-term memory and alleviate the vanishing gradient problem existing in conventional RNN (Bengio et al., 1994; Pascanu et al., 2013).

The bi-LSTM is an extension to LSTM, and it makes the neural network learn the sequence information in both forward (past to future) and backward (future to past) directions and makes the model more robust. The schematic of a bi-LSTM system with one LSTM layer and one dense layer in the hidden layer is shown in Figure 2.

In this study, the deep learning methods were built on top of the PyTorch, which is a recent addition to the ecosystem of the deep learning framework (Ketkar, 2017). In developing the LSTM and bi-LSTM models, the RMSE and Adaptive Moment Estimation (Adam) were used as the loss function and optimizer. Hyperparameters (e.g., the number of the LSTM layers, the number of the neurons in every LSTM unit, the number of the neurons in the hidden layer, the number of the training epoch, and the batch size) were optimized to improve the learning performance, and the RMSE was used as the optimization criterion.

$$\text{RMSE} = \sqrt{\frac{\sum_{i=1}^{n}(x_i - \hat{x}_i)^2}{n}} \tag{6}$$

where n is the size of the validation data; $\hat{x}_i$ and x_i represents the predicted and observed VTEC values, respectively.

The optimal network structures of the LSTM and bi-LSTM models were determined after many experiments. In this research, DOY$_s$, DOY$_c$, HOD$_s$, HOD$_c$, Glon, Glat, F10.7, Dst, and VTEC at one epoch were considered as an independent variable vector. The variable vectors of the previous 24 hr were used as input data for the LSTM and bi-LSTM models. The input data pass through two LSTM layers and one dense layer (with 28 neurons) and then get the output data (VTECs in the 25th and 26th hr) in the development of the LSTM model. Similarly, the architecture of the bi-LSTM model includes the same input layer as that of the LSTM model, two bidirectional LSTM layers, one dense layer (with 15 neurons), and the predicted VTECs (in the 25th and 26th hr) in the output layer.

To assess the performance of the models, four other evaluation metrics were also used in this study: mean error (mean), the standard deviation of the residuals (σ), mean absolute error (MAE), and Pearson correlation coefficient (Corr).

$$\text{Mean} = \frac{1}{N}\sum_{i=1}^{N}(x_i - \hat{x}_i) \tag{7}$$

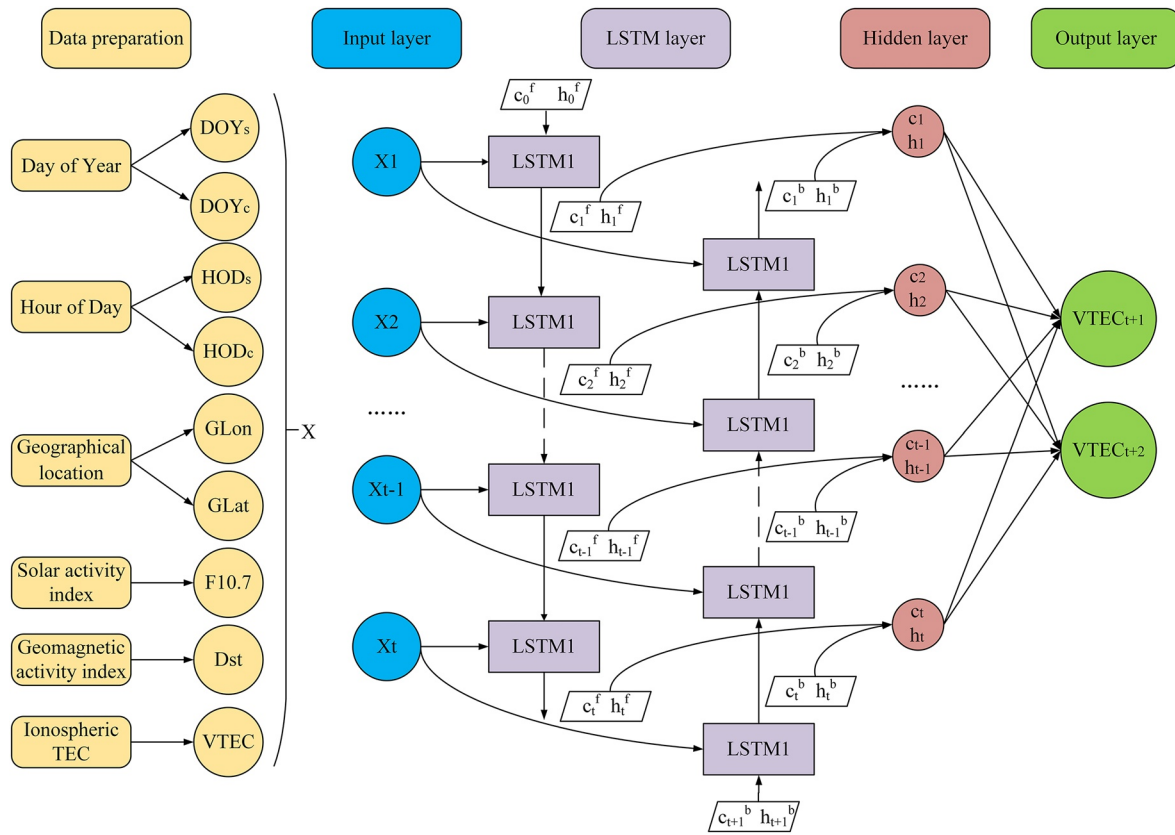$$\text{MAE} = \frac{1}{N}\sum_{i=1}^{N}|x_i - \hat{x}_i| \tag{8}$$

Figure 2. Schematic of a bi-LSTM system with one LSTM layer and one dense layer in the hidden layer. DOY_s and DOY_c are the sine and cosine components of day of year; HOD_s and HOD_c are the sine and cosine components of hour of day; GLon and GLat are for geographic longitude and latitude, respectively; X_t is the independent variable set at the tth epoch; h and c are the temporary results and memory cells, respectively; VTEC, vertical total electron content. LSTM, long short-term memory; and bi-LSTM, bidirectional long short-term memory.

$$\text{Corr} = \frac{\sum_{i=1}^{N}\left(\widehat{x}_i - \overline{\widehat{x}}\right)\left(x_i - \overline{x}\right)}{\sqrt{\sum_{i=1}^{N}\left(\widehat{x}_i - \overline{\widehat{x}}\right)^2}\sqrt{\sum_{i=1}^{N}\left(x_i - \overline{x}\right)^2}} \tag{9}$$

$$\sigma = \sqrt{\frac{\sum_{i=1}^{N}\left((x_i - \hat{x}_i) - \text{mean}\right)^2}{N-1}} \tag{10}$$

where N is the total number of data samples; $\overline{\widehat{x}}$ and $\overline{x}$ are the mean values of $\widehat{x}_i$ and x_i, respectively.

4. Results

Measurements from the 12 stations (marked with red dots in Figure 1) were used for test purposes to evaluate the spatial performance of the new model. Observations from all the remaining stations were sequentially divided into three groups: training data set (from 1 January 2018 to 31 December 2020), cross-validation data set (from 1 January 2021 to 31 May 2021), and test data set (from 1 June 2021 to 31 December 2021). The out-of-sample measurements (test data set) were used as an external reference to evaluate the accuracy of the models.
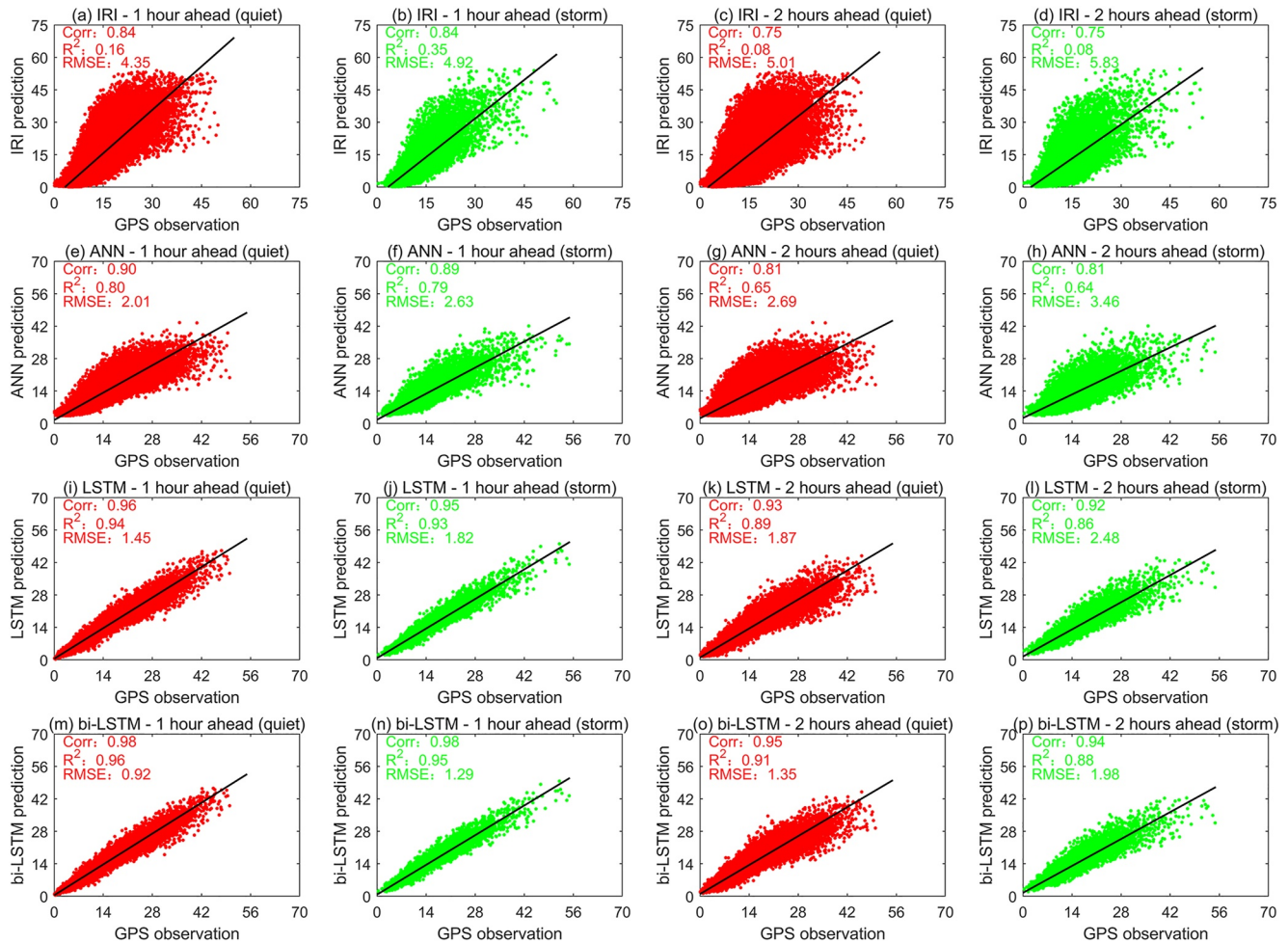
Figure 3. Scatter plots of VTECs estimated from GPS data versus predicted ones from the IRI-2016, ANN, LSTM, and bi-LSTM models on the test data set. The red and green points denote geomagnetic quiet and storm conditions, respectively. GPS, Global Positioning System; VTEC, vertical total electron content; IRI, International Reference Ionosphere; ANN, artificial neural network; LSTM, long short-term memory; and bi-LSTM, bidirectional long short-term memory.

4.1. Model Performance

In this section, the performance of the proposed model was evaluated based on the test set. Figure 3 shows the correlation between the VTECs obtained from the GPS data and predicted ones from each of the IRI-2016, ANN, LSTM, and bi-LSTM models under geomagnetic quiet (Dst ≥ −20 nT) and storm (Dst ≤ −50 nT) conditions. In each panel, the black line is the linear function fitting the VTEC points of the panel and the listed three statistical indicators are: Corr, the coefficient of determination (R^2), and RMSE. The red and green points denote the geomagnetic quiet and storm conditions, respectively. The first column shows the results of the 1 hr ahead predictions under geomagnetic quiet conditions resulting from the IRI-2016 (Figure 3a), ANN (Figure 3e), LSTM (Figure 3i), and bi-LSTM (Figure 3m) methods. It can be seen that the performance of the deep learning models is better than that of the IRI-2016 model. Moreover, the scatter plot of the ANN model is more spread away from the diagonal (RMSE = 2.01 TECU) compared with the LSTM (RMSE = 1.45 TECU) and bi-LSTM (RMSE = 0.92 TECU) models, and the bi-LSTM model fits best to the GPS measured VTEC with the highest correlation (0.98) and lowest RMSE value. Similar to the first column, the second column shows the results under geomagnetic storm conditions. The Corr in the second column is slightly smaller than that of the first column in the same row, while the RMSE in the second column is larger than that of the first column in the same row. This implies that it is more challenging to model the ionospheric TEC under geomagnetic storm conditions. The third column is for the results of the 2 hr ahead predictions under geomagnetic quiet conditions. It depicts that the Corr decreases and the RMSE increases for all the four models as we predict further into the future. The fourth column further
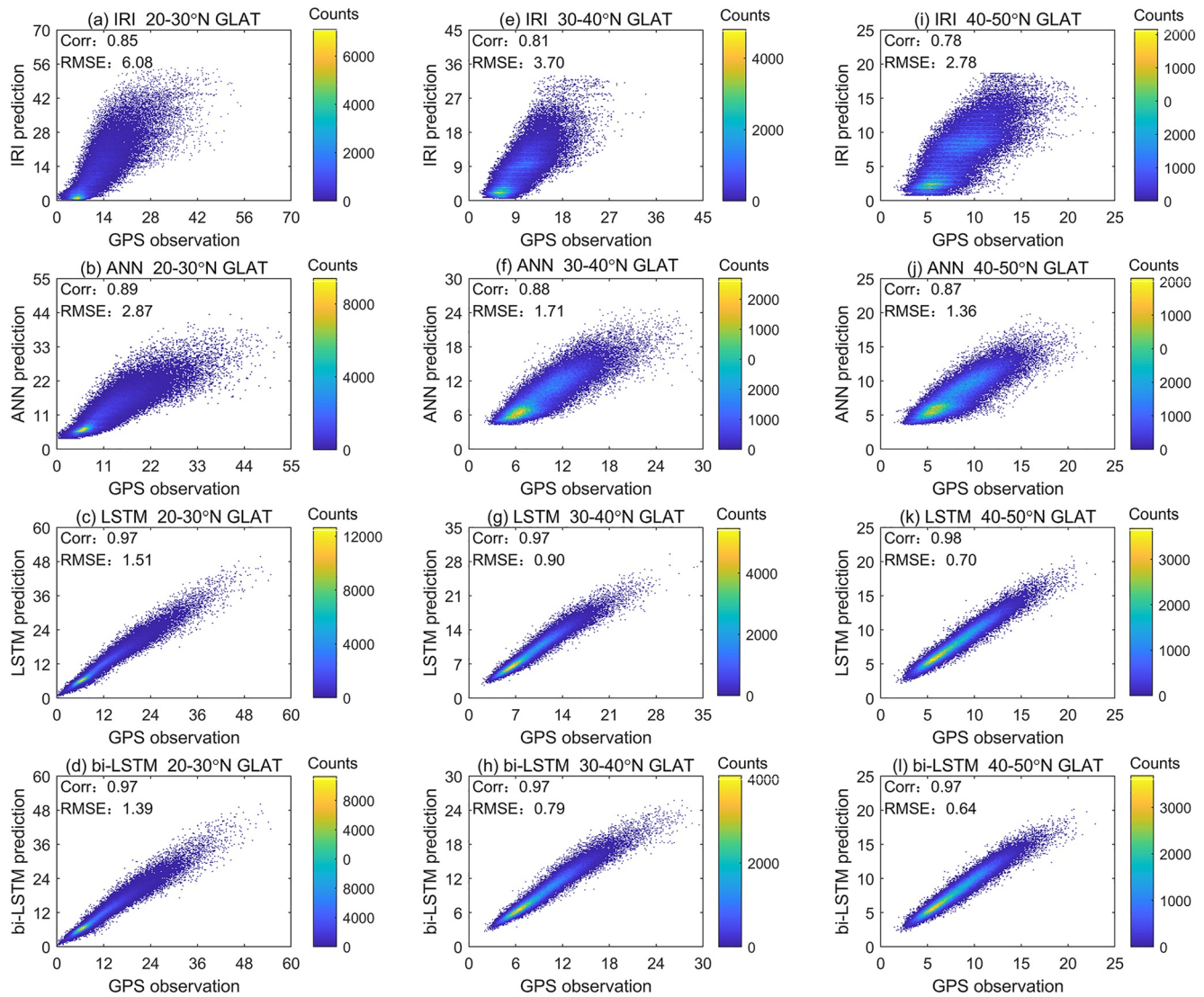
Figure 4. Binned scatter plots of VTECs estimated from GPS data versus the 1 hr ahead predicted ones from the IRI-2016, ANN, LSTM, and bi-LSTM models on the test data set with geographic latitudinal ranges of 20°N~30°N (first column), 30°N~40°N (second column), and 40°N~50°N (third column). IRI, International Reference Ionosphere; ANN, artificial neural network; LSTM, long short-term memory; bi-LSTM, bidirectional long short-term memory; GPS, Global Positioning System; and RMSE, root mean square error.

demonstrates that the prediction results of all the four models under geomagnetic storm conditions are worse than that under geomagnetic quiet conditions. Furthermore, statistical results of the residuals (estimated-observed) on the test data set show that the RMSE of the IRI-2016, ANN, LSTM, and bi-LSTM models for the 1 hr ahead predictions are 4.40, 2.23, 1.65, and 1.12 TECU, respectively, which are 14%, 25%, 24%, and 33% smaller than the corresponding RMSE of the 2 hr ahead predictions. The root mean square errors (RMSEs) of the 1 and 2 hr ahead predictions from the bi-LSTM model are, respectively, 75/50/32% and 72/48/22% smaller than that of the IRI-2016, ANN, and LSTM models. These results all suggest that the bi-LSTM model is the best performer.

All the CMONOC stations were then subdivided into three latitudinal zones: 20°N~30°N, 30°N~40°N, and 40°N~50°N geographic latitude (GLAT) regions. Figure 4 shows the statistical results of the 1 hr ahead predictions resulting from the IRI-2016, ANN, LSTM, and bi-LSTM models at the above three latitudinal zones. Generally, the models based on deep learning methods outperform the IRI-2016 model. For example, in the region 20°N~30°N GLAT (Figures 4a–4d), the RMSE of the IRI-2016, ANN, LSTM, and bi-LSTM models are 6.08, 2.87, 1.51, and 1.36 TECU, respectively, and their corresponding correlation coefficients are 0.85, 0.89, 0.97, and 0.97, which means the prediction accuracy of bi-LSTM improves 78%, 53%, and 10% over the IRI-2016, ANN,

Table 2
Statistical Values of the Residuals Between the 1 hr Ahead Predictions of the Bi-LSTM Model and the GPS Observed Ones on the Test Data Set

Regions	Quiet time				Storm time			
	mean	σ	RMSE	MAE	mean	σ	RMSE	MAE
20°N~30°N	0.13	1.25	1.25	0.86	0.36	1.67	1.71	1.17
30°N~40°N	−0.02	0.76	0.76	0.56	0.16	1.10	1.12	0.80
40°N~50°N	0.04	0.61	0.62	0.47	0.20	0.90	0.92	0.68
20°N~30°N, day	0.18	1.68	1.69	1.21	0.25	2.05	2.07	1.53
20°N~30°N, night	0.13	0.90	0.91	0.66	0.25	1.05	1.08	0.78
30°N~40°N, day	−0.01	0.90	0.90	0.67	0.26	1.23	1.26	0.97
30°N~40°N, night	−0.004	0.66	0.66	0.50	0.10	0.84	0.84	0.62
40°N~50°N, day	0.07	0.65	0.66	0.51	0.32	0.93	0.98	0.77
40°N~50°N, night	0.03	0.59	0.59	0.45	0.10	0.75	0.76	0.57

Note. Cells with green and orange shading show the minimum and maximum values of the MAE, respectively. bi-LSTM, bidirectional long short-term memory; GPS, Global Positioning System; MAE, mean absolute error; RMSE, root mean square error; and σ, standard deviation.

and LSTM, respectively. Similar performance can be found in the other two regions. For example, the RMSEs of the bi-LSTM model in the two regions 30°N~40°N/40°N~50°N GLAT are 0.79/0.64 TECU, which are 79/77%, 54/53%, and 12/8% smaller than that of the IRI-2016, ANN, and LSTM models. The accuracy improvement (over the IRI-2016, ANN, and LSTM models) of the bi-LSTM model in the region 30°N~40°N GLAT is greater than those in the regions within the 20°N~30°N GLAT and 40°N~50°N GLAT. This is possibly due to the fact that the coverage of the CMONOC stations (115 stations) within the 30°N~40°N GLAT is much denser than that within the 20°N~30°N GLAT (71 stations) and 40°N~50°N GLAT (54 stations). For the four models, the accuracy within 40°N~50°N GLAT is better than that within 30°N~40°N GLAT, while the worst is within 20°N~30°N GLAT. This regional difference can be related to the significant ionospheric variability over low latitudes. Results for the 2 hr ahead predictions are shown in Figure S1 in Supporting Information S1, from which a similar variation pattern can be observed, and the magnitude of the Corr value is slightly smaller than that in Figure 4 under the same condition, while the magnitude of the RMSE value is slightly bigger.

Table 2 summarizes the characteristics of the residuals between the 1 hr ahead predictions resulting from the bi-LSTM model and the GPS observed ones on the test data set in the form of mean, σ, RMSE, and MAE values. The results for the three latitudinal zones under geomagnetic quiet/storm conditions and daytime (10:00–18:00 LT)/nighttime (19:00–09:00 LT) conditions are given. The cells with green and orange shading are the minimum and maximum MAE, respectively. For geomagnetic quiet conditions, the mean value is around zero and the maximum value (0.18 TECU) is within 20°N~30°N GLAT during daytime. The σ and RMSE values are found 0.90–1.69 TECU, 0.66–0.90 TECU, and 0.59–0.66 TECU within the 20°N~30°N, 30°N~40°N, and 40°N~50°N GLAT, respectively. Moreover, the minimum MAE (0.45 TECU) is found in the region 40°N~50°N GLAT during nighttime, while the maximum MAE (1.21 TECU) is within the 20°N~30°N GLAT during daytime. Under geomagnetic storm conditions, the mean values increase and the σ and RMSE values 1.05–2.07, 0.84–1.26, and 0.75–0.98 TECU are found in the regions within the 20°N~30°N, 30°N~40°N, and 40°N~50°N GLAT, respectively. The minimum (0.57 TECU) and maximum (1.53 TECU) values of the MAE are also found during nighttime within the 40°N~50°N GLAT region and daytime within the 20°N~30°N GLAT region with an increment of 27% and 26%, compared with the corresponding values under geomagnetic quiet conditions. Furthermore, Table 2 shows that the bi-LSTM model performs better during nighttime than daytime. Similar results for the 2 hr ahead predictions are shown in Table S1 in Supporting Information S1.

The variation of the RMSE, MAE, Corr, and R^2 for the 1 hr ahead predictions resulting from the IRI-2016, ANN, LSTM, and bi-LSTM models at each of the 12 test stations shown in Table 1 are presented in Figure 5. It can be seen from Figure 5a that at each station the RMSE of the IRI-2016 model is much larger than that of the other models; the RMSE of the LSTM and bi-LSTM models are smaller than that of the ANN model; the RMSE of the bi-LSTM model is the smallest; the RMSE of the IRI-2016, ANN, LSTM, and bi-LSTM models are found in the ranges 2.30–7.21, 1.28–3.85, 0.83–2.18, and 0.63–1.98 TECU, respectively; the RMSE of the four models increase with the decrease of latitudes. The MAE in Figure 5b shows the same variation trend as that of the RMSE, and for the IRI-2016, ANN, LSTM, and bi-LSTM models, their MAE values are found in the
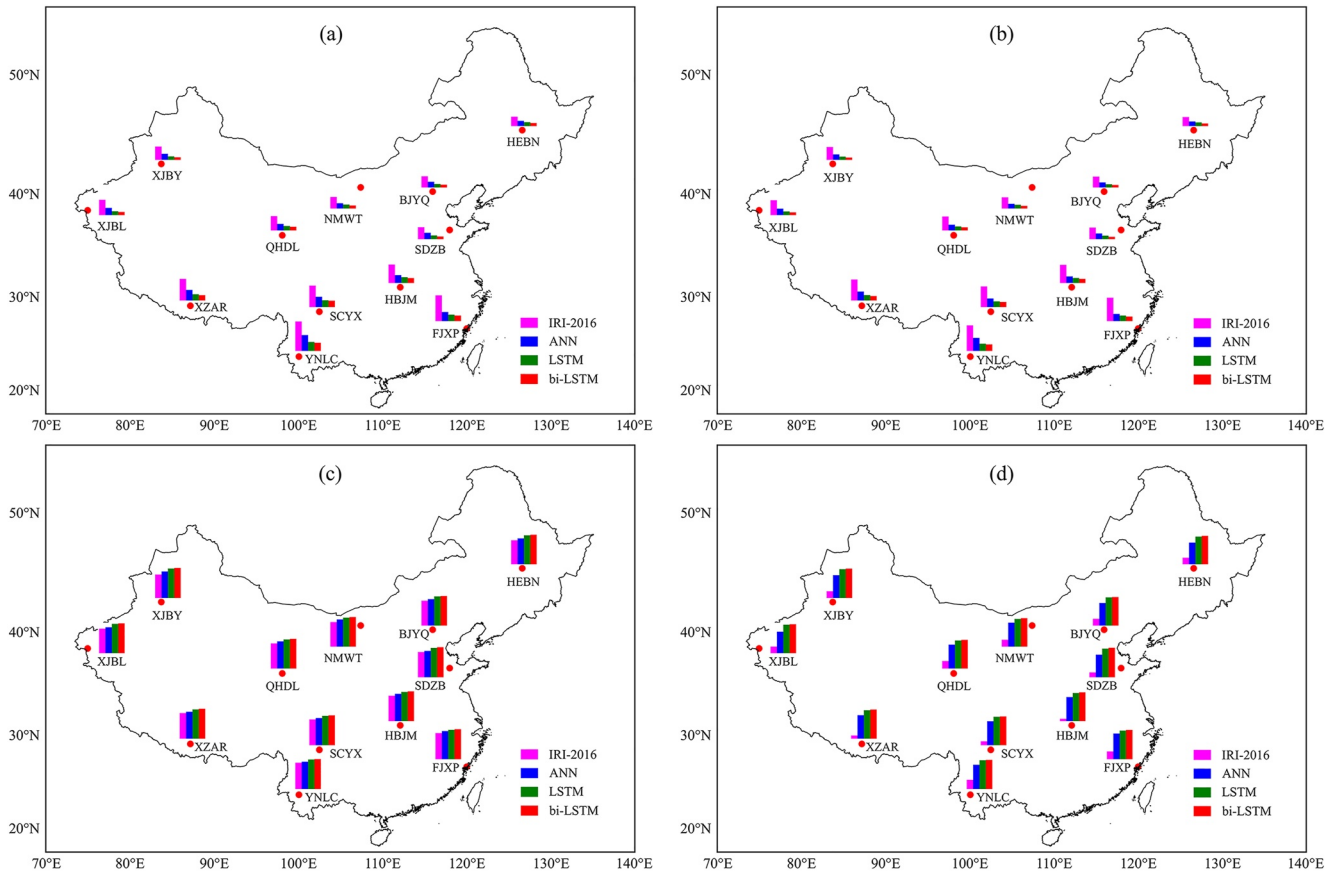
Figure 5. Bar maps of (a) RMSE, (b) MAE, (c) correlation coefficient (Corr), and (d) coefficient of determination (R^2) for the 1 hr ahead predictions resulting from the IRI-2016, ANN, LSTM, and bi-LSTM models. RMSE, root mean square error; MAE, mean absolute error; GPS, Global Positioning System; IRI, International Reference Ionosphere; ANN, artificial neural network; LSTM, long short-term memory; and bi-LSTM, bidirectional long short-term memory.

ranges 1.92–5.40, 0.98–2.76, 0.68–1.57, and 0.48–1.37 TECU, respectively. Figure 5c depicts that the Corr of the IRI-2016 model (0.76–0.86) is smaller than that of the ANN model (0.84–0.92), the LSTM model (0.94–0.96), and the bi-LSTM model (0.96–0.98) at each station. The R^2 of the IRI-2016, ANN, LSTM, and bi-LSTM models shown in Figure 5d are found in the ranges 0.07–0.30, 0.70–0.84, 0.90–0.94, and 0.93–0.96, respectively. More-over, the Corr and R^2 show a fluctuating trend with the decrease of latitudes. In summary, the bi-LSTM model outperforms the other two deep learning models and also the IRI-2016 model at all the 12 test stations. Also, the prediction accuracy of the bi-LSTM model increases with the increase of latitude, while the prediction accuracies in the same latitude zone have little difference. Similar results for the 2 hr ahead predictions are shown in Figure S2 in Supporting Information S1.

4.2. Variation of Model Performance With Local Time

Figure 6 shows the mean diurnal variation of the VTECs estimated from GPS data and 1 hr ahead predictions resulting from the IRI-2016, ANN, LSTM, and bi-LSTM models at the aforementioned 12 test stations, and the hourly RMSE is also provided. In each panel, the horizontal axis, the left vertical axis, and the right vertical axis represent the local time, the values of VTEC and RMSE, respectively. The stations that are in the first, second, and third rows are located within the 40°N~50°N, 30°N~40°N, and 20°N~30°N GLAT, respectively, and the stations of the same row are arranged from west to east, according to their longitude. It can be seen from the first row that results of the IRI-2016 model are significantly larger than the GPS estimated VTEC values at stations NMWT (during 13–14 LT hr), BJYQ (during 13–15 LT hr), and HRBN (during 11–15 LT hr), meaning the over-estimation of the IRI-2016 model; whereas at station XJBY, it underestimates the GPS estimated VTEC during all the LT hours. The ANN model underestimates the GPS estimated VTECs before noon and overestimates from
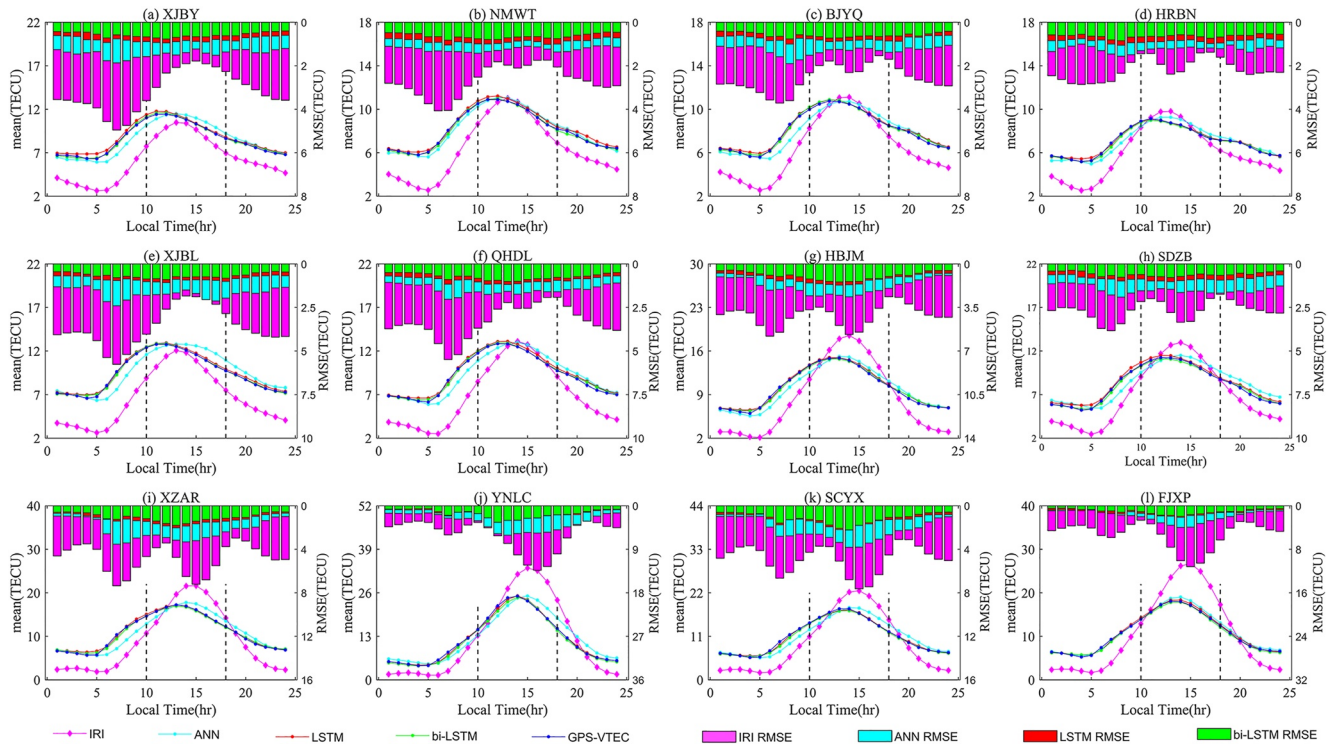
Figure 6. Mean diurnal variations of the VTEC estimated from GPS data and the 1 hr ahead predictions resulting from the IRI-2016, ANN, LSTM, and bi-LSTM models at stations (a) XJBY, (b) NMWT, (c) BJYQ, (d) HRBN, (e) XJBL, (f) QHDL, (g) HBJM, (h) SDZB, (i) XZAR, (j) YNLC, (k) SCYX, and (l) FJXP. The hourly RMSE of the residuals for each model is also shown in the figure. The two vertical dashed lines in each panel denote the start and end moments of the daytime. GPS, Global Positioning System; VTEC, vertical total electron content; IRI, International Reference Ionosphere; ANN, artificial neural network; LSTM, long short-term memory; bi-LSTM, bidirectional long short-term memory; and RMSE, root mean square error.

noon until midnight at all the four stations. In contrast, the LSTM model follows the VTEC variation pattern well for each LT hour, and the bi-LSTM model fits the GPS estimated VTECs the best as its RMSE at each LT hour is the smallest.

It can be seen from the second (Figures 6e–6h) and third (Figures 6i–6l) rows that in the regions within the 30°N∼40°N and 20°N∼30°N GLAT, the time length for the overestimation of the VTECs by the IRI-2016 model is more extended than that within the 40°N∼50°N GLAT. For example, at stations QHDL (during 14–16 LT hr), HBJM (during 12–18 LT hr), and SDZB (during 12–17 LT hr) located within the 30°N∼40°N GLAT and at stations XZAR (during 13–18 LT hr), YNLC (during 13–20 LT hr), SCYX (during 13–19 LT hr), and FJXP (during 11–19 LT hr) located within the 20°N∼30°N GLAT, the overestimation is more pronounced. In addition, as shown in Figures 6e–6l, the ANN model underestimates the VTEC before peak hours and overestimates after peak hours until dawn hours. However, the ANN model outperforms the IRI-2016 model. Furthermore, the VTEC resulting from the LSTM and bi-LSTM models agrees well with the diurnal variations of the GPS estimated VTEC, and the bi-LSTM model outperforms the LSTM, which is evident from the RMSE bars shown in Figures 6e–6l. The RMSE variation in Figure 6 shows that at higher latitude stations (e.g., stations XJBY, NMWT, BJYQ, HRBN, XJBL, and QHDL), it increases with the increase/decrease of VTEC values at dawn/dusk hours and it decreases during daytime hours; at lower latitude stations, it reaches the maximum value when the VTEC value reaches the peak, for example, at stations YNLC and FJXP or it shows two peaks, for example, at stations HBJM, SDZB, XZAR, and SCYX. Similar results for the 2 hr ahead predictions are shown in Figure S3 in Supporting Information S1.

For statistical analyses, the 10:00–18:00 LT and 19:00–09:00 LT periods were selected to represent daytime and nighttime, respectively. The RMSE of the residuals for the 1 hr ahead predictions resulting from the IRI-2016, ANN, LSTM, and bi-LSTM models during the daytime and nighttime periods are shown in Table 3. We can see from Table 3 that for the ANN, LSTM, and bi-LSTM models, the RMSE during nighttime is smaller than that

Table 3
RMSE of the Residuals of the 1 hr Ahead Predictions Resulting From the IRI-2016, ANN, LSTM, and Bi-LSTM Models During the Daytime and Nighttime Periods

Station code	IRI-2016		ANN		LSTM		bi-LSTM	
	Daytime	Nighttime	Daytime	Nighttime	Daytime	Nighttime	Daytime	Nighttime
XJBY	2.25	3.84	1.40	1.48	0.88	0.75	0.67	0.53
NMWT	2.01	3.18	1.25	1.24	0.93	0.85	0.72	0.60
BJYQ	1.96	3.00	1.29	1.33	0.84	0.72	0.66	0.55
HRBN	1.83	2.45	1.18	1.27	0.89	0.86	0.64	0.64
XJBL	2.56	4.41	1.81	1.68	0.95	0.80	0.78	0.61
QHDL	2.45	3.97	1.62	1.43	1.08	0.85	0.90	0.64
HBJM	4.26	4.28	2.31	1.58	1.46	1.05	1.26	0.79
SDZB	2.52	2.87	1.57	1.45	0.94	0.78	0.68	0.55
XZAR	5.20	4.96	2.86	2.07	1.66	1.06	1.42	0.87
YNLC	9.74	4.18	5.36	2.31	2.46	1.26	2.39	1.13
SCYX	5.62	4.74	3.14	1.85	1.73	1.08	1.63	0.94
FJXP	7.94	4.19	3.11	1.27	1.69	1.05	1.51	0.78

Note. RMSE, root mean square error; IRI, International Reference Ionosphere; ANN, artificial neural network; LSTM, long short-term memory; and bi-LSTM, bidirectional long short-term memory.

during daytime at most stations. For the IRI-2016 model, the RMSE of nighttime is larger than daytime at the stations within the 40°N~50°N and 30°N~40°N GLAT. It is also evident that compared with the other three models, the bi-LSTM model performs the best during both daytime and nighttime. Similar results for the residuals of the 2 hr ahead predictions are shown in Table S2 in Supporting Information S1.

4.3. Variation of Model Performance With Season

The hourly mean of the VTECs estimated from GPS data, the 1 hr ahead predictions resulting from the four selected models, and the corresponding hourly RMSE of the residuals in the equinox (March, April, September, and October), winter (January, February, November, and December), and summer (May, June, July, and August) were calculated for evaluating the performance of the bi-LSTM model in different seasons. Figure 7 shows the results at three representative stations located within the 40°N~50°N, 30°N~40°N and 20°N~30°N GLAT. It can be seen that the IRI-2016 model overestimates the VTEC during the period from the peak to dusk hours, except for station BJYQ in the summer season, and the overestimation is more notable in the equinox seasons. Compared with the ANN (cyan) and LSTM (red) predictions, the bi-LSTM prediction (green) is the closest to the GPS estimated VTEC (blue) during all the seasons. The RMSE bar in Figure 7 shows that the RMSE of the bi-LSTM model is slightly smaller than that of the LSTM model. The LSTM model outperforms the ANN and IRI-2016 models. Similar results for the 2 hr ahead predictions are shown in Figure S4 in Supporting Information S1.

4.4. Model Performance Under Geomagnetic Quiet and Storm Conditions

A moderate geomagnetic storm occurred late on 27 September 2020 and lasted until September 28 was selected for the investigation of the new model's performance under geomagnetic quiet and storm conditions. The plots of the GPS-VTEC and the 1-hr ahead predictions resulting from the IRI-2016, ANN, LSTM, and bi-LSTM models at the 12 test stations are shown in Figure 8. It can be observed that the IRI-2016 model shows a minor overestimation of the GPS-measured VTECs at peak hours at the stations that are within the 40°N~50°N and 30°N~40°N GLAT, except for the station HBJM and an evident underestimation during 20–12 LT hr at all the stations. The ANN (cyan), LSTM (red), and bi-LSTM (green) models show a similar variation trend with the GPS-VTEC (blue). Nevertheless, the ANN model cannot reflect the fluctuations of the VTEC. The LSTM and bi-LSTM models respond well to the arrival of the geomagnetic storm and reflect the steep rise and sudden fall well, for example, the variations from 23 LT of September 27 to 12 LT of September 28.
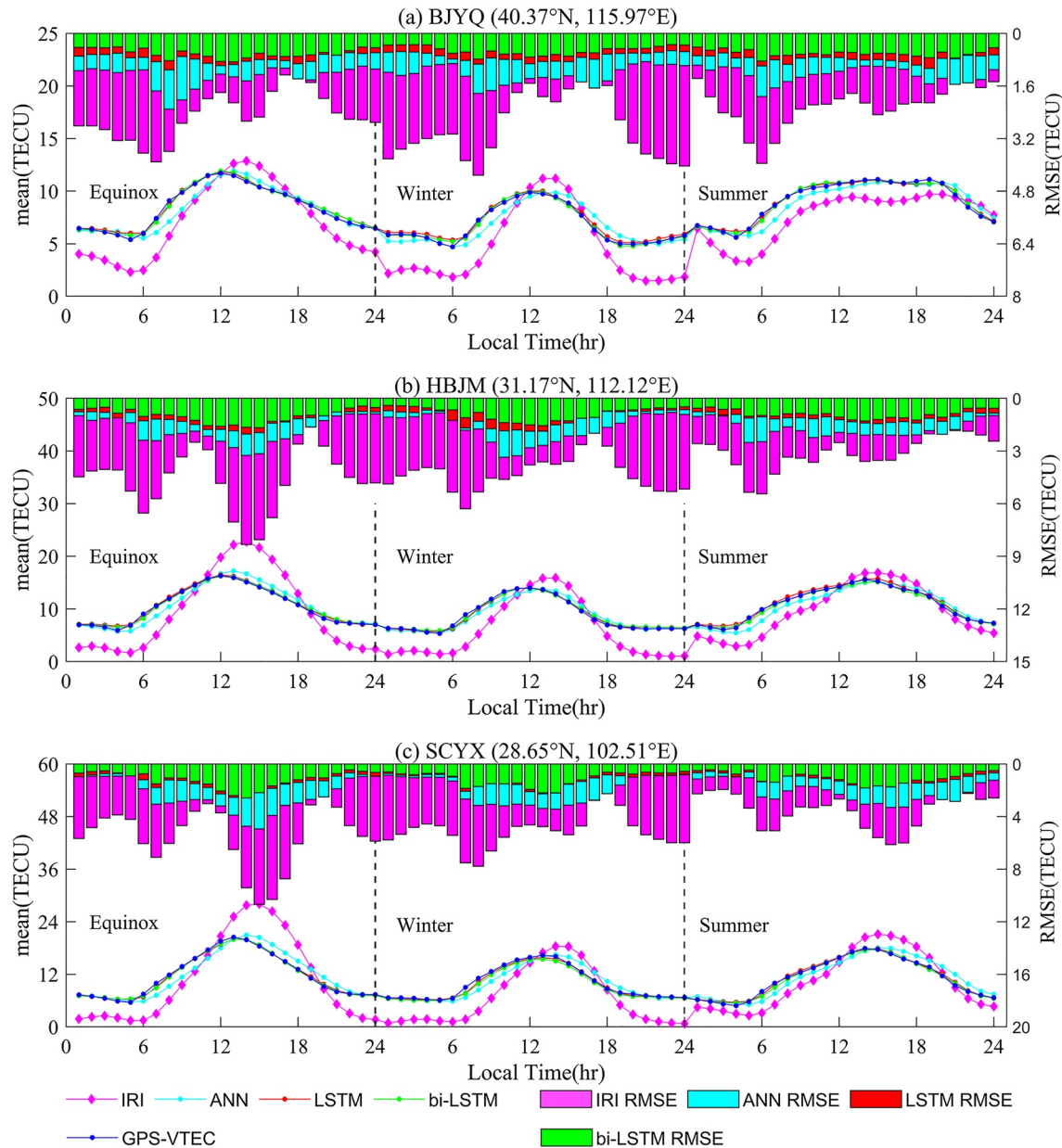
Figure 7. Seasonal variations of the VTECs estimated from GPS data and 1 hr ahead predictions resulting from the IRI-2016, ANN, LSTM, and bi-LSTM models at stations (a) BJYQ, (b) HBJM, and (c) SCYX. The hourly RMSE of the residuals during the equinox, winter, and summer are also plotted. GPS, Global Positioning System; VTEC, vertical total electron content; IRI, International Reference Ionosphere; ANN, artificial neural network; LSTM, long short-term memory; bi-LSTM, bidirectional long short-term memory; and RMSE, root mean square error.

4.5. Comparison With GIMs From the Chinese Academy of Sciences (CAS)

In this section, the GIMs obtained from the Chinese Academy of Sciences (CAS) were used as the reference to assess the accuracy of the new model. The GIMs are generated using the Spherical Harmonic (SH) expansion plus Generalized Trigonometric Series function (SHPTS) by the CAS (Li et al., 2015). The quality of the GIMs has been assessed using GPS differential STECs and the Jason VTECs as the references (Li et al., 2015, 2021; Liu et al., 2018; Ren et al., 2019). For comparison, the 1 and 2 hr ahead predicted VTEC maps with a resolution of 2.5° × 5° were obtained using the bi-LSTM model. Figure 9 shows the RMSE map for the 1 hr ahead predictions on the test data set (from 1 June 2021 to 31 December 2021). Figure 9 reveals that in the south of China
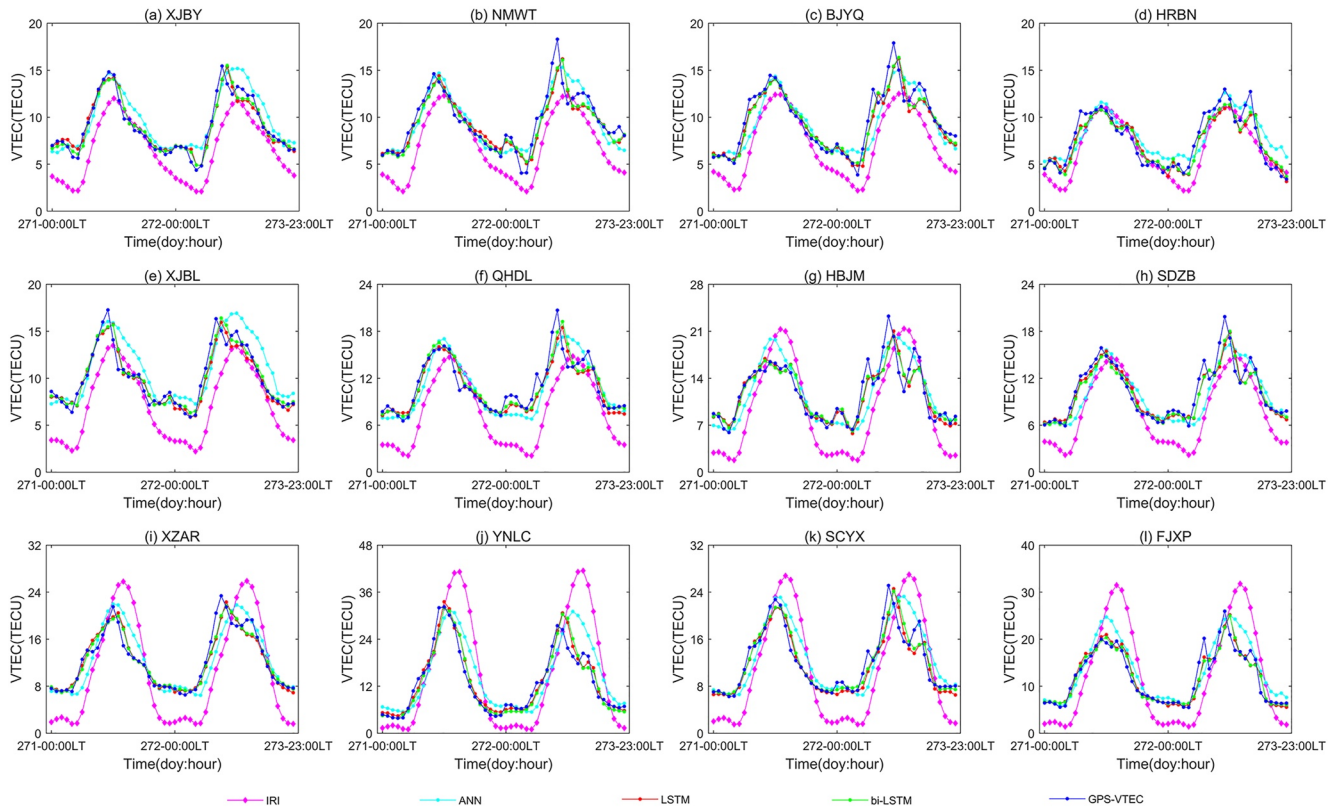
Figure 8. Performance of the IRI-2016 (magenta), ANN (cyan), LSTM (red), and bi-LSTM (green) models during 27–28 September 2020. The blue lines are for the GPS measured VTEC. IRI, International Reference Ionosphere; ANN, artificial neural network; LSTM, long short-term memory; and bi-LSTM, bidirectional long short-term memory.

(e.g., Guangdong, Guangxi, and Yunnan provinces), the bi-LSTM model performs worse than in the north of China. This is an expected result because the south of China is part of the equatorial anomaly region, and significant VTEC variations generally occur in this region. The RMSE of the bi-LSTM model in the north of China region is small and primarily within 1.5 TECU. The RMSE map of the 2 hr ahead predictions shown in Figure S5
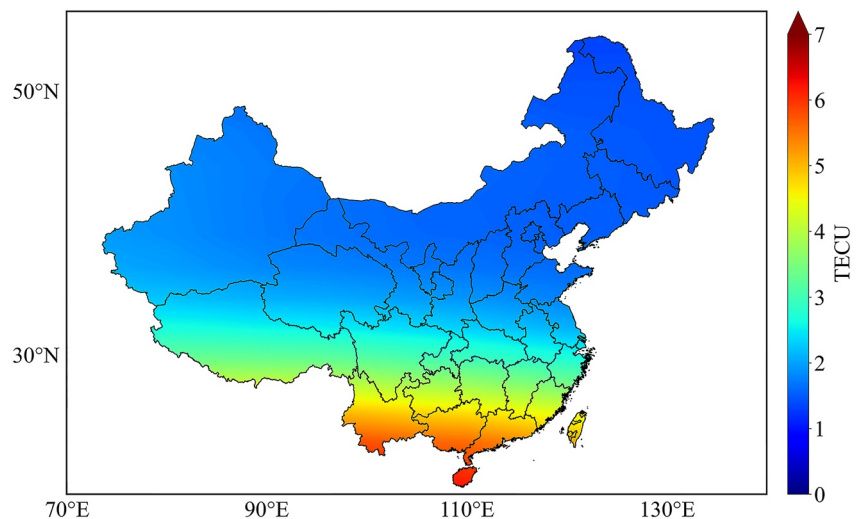

Figure 9. Spatial distribution of the RMSE (unit: TECU) of the 1 hr ahead predictions using the CAS GIMs as the reference. RMSE, root mean square error; CAS, Chinese Academy of Sciences; and GIMs, global ionospheric maps.
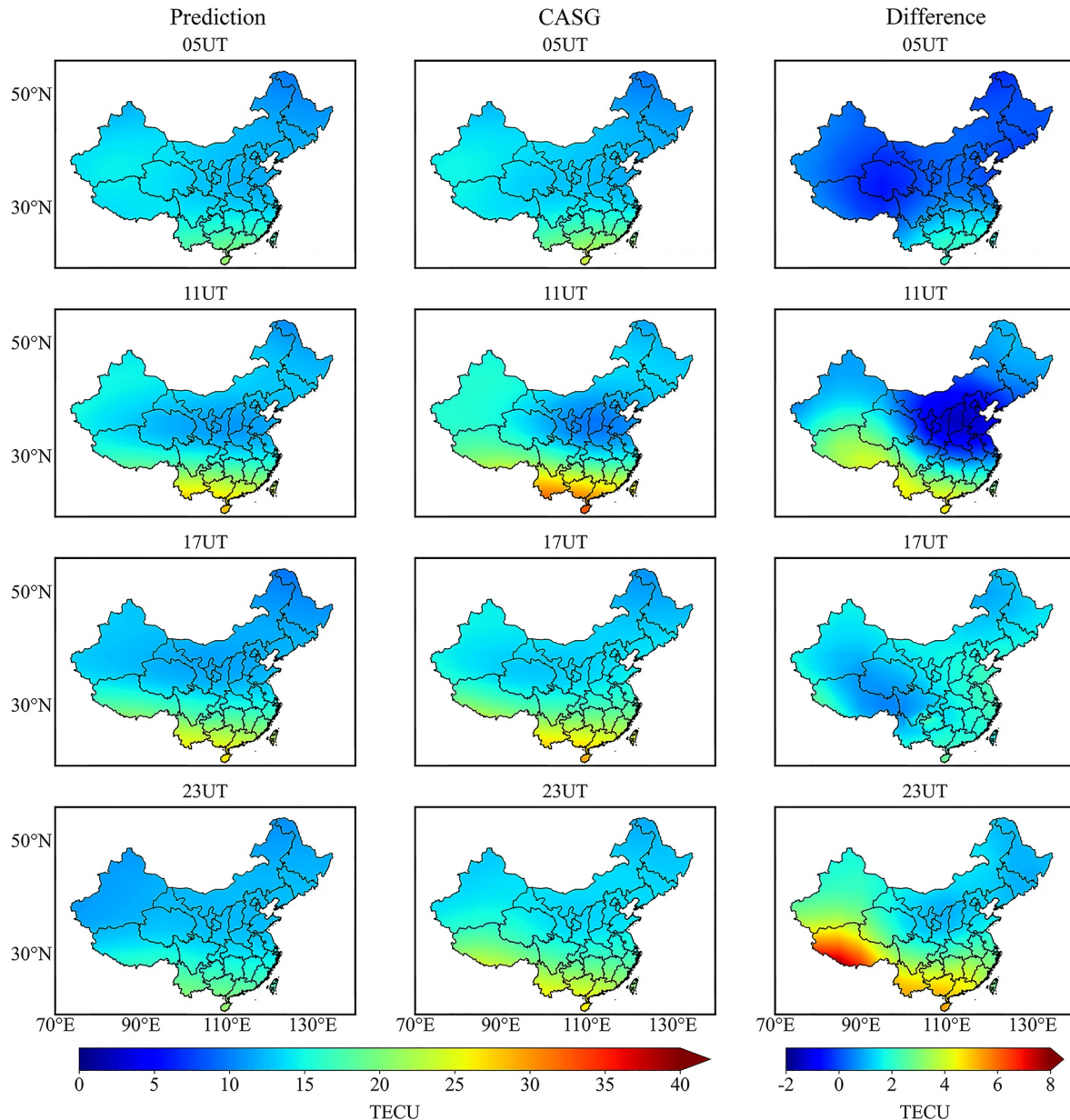
Figure 10. Snapshots of the 1 hr ahead predicted VTEC maps resulting from the bi-LSTM model (first column) and CAS GIMs (second column) along with their differences (third column) at 05, 11,17, and 23 UT under geomagnetic quiet (25 May 2021) conditions. VTEC, vertical total electron content; bi-LSTM, bidirectional long short-term memory; CAS, Chinese Academy of Sciences; and GIMs, global ionospheric maps.

in Supporting Information S1 depicts the same spatial variation characteristics with slightly larger RMSEs than those shown in Figure 9.

The results of comparisons between the 1 hr ahead predicted TEC maps generated from the bi-LSTM model and the CAS GIMs for randomly selected geomagnetic quiet (25 May 2021) and storm (4 November 2021) days are shown in Figures 10 and 11, respectively. It should be noted that the ground-based GPS data on the geomagnetic quiet and storm days are not used in the training process of the bi-LSTM model. The first, second, and third columns are the maps of the bi-LSTM model predictions, CAS GIMs, and their differences, respectively. The first and second columns of Figure 10 indicate that the predicted TEC maps agree well with that of the CAS. The third column of Figure 10 shows that at 5:00 and 11:00 UT, the differences between the first and second column in the same row are smaller, mostly within 1 TECU with an exception for parts of southern and southwest China
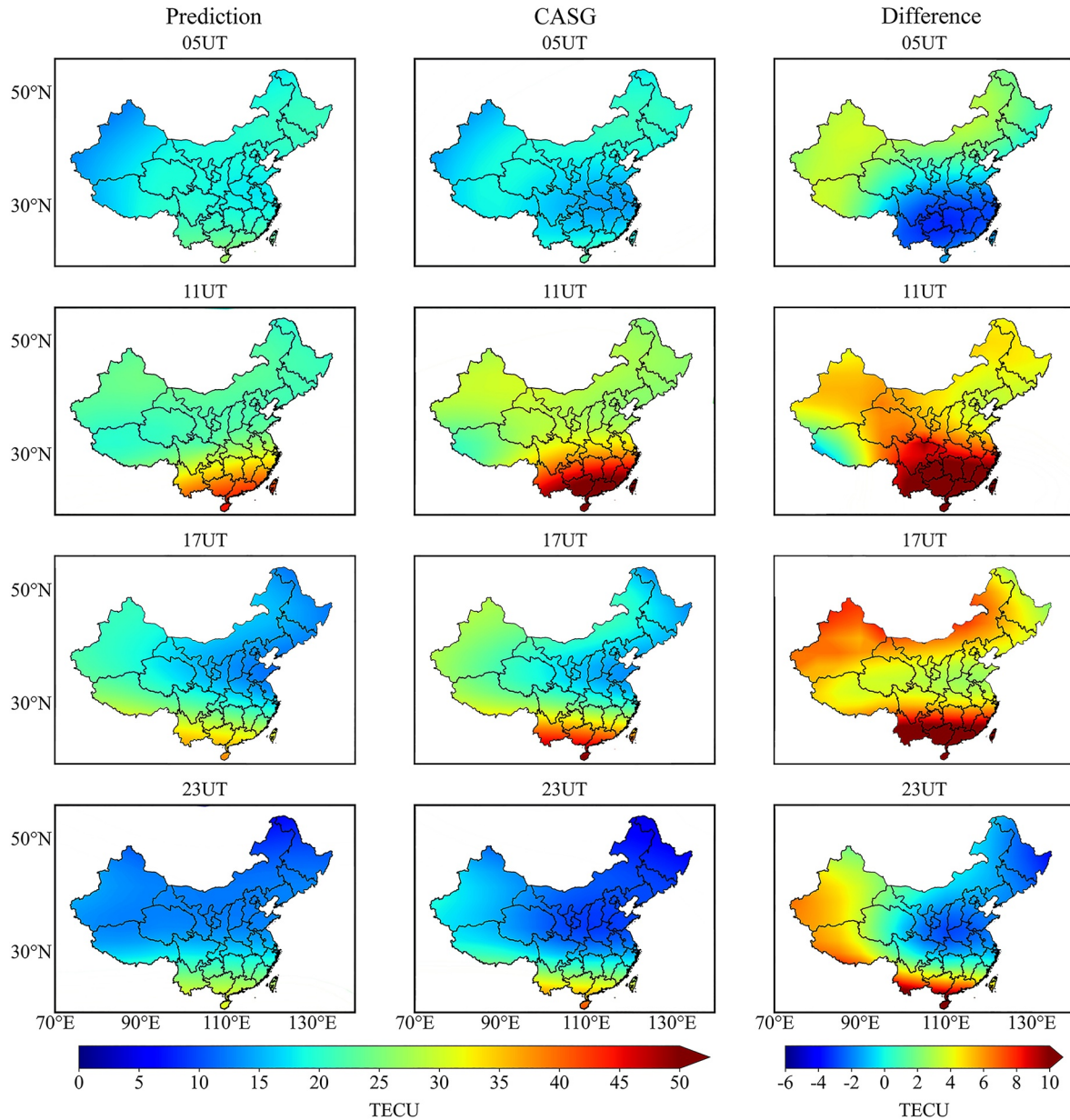
Figure 11. Similar to Figure 10 but for geomagnetic storm (4 November 2021) conditions.

at 11:00 UT; at 17:00 and 23:00 UT, the differences are slightly larger than that at 5:00 and 11:00 UT and except for parts of southern and southwest China at 23:00 UT, the majority of the differences are within 2 TECU.

Figure 11 shows that the predicted TEC maps also show good agreement with that of the CAS during the strong geomagnetic storm periods. It can be seen from the first and second columns that compared with TEC maps under geomagnetic quiet conditions, the ionospheric TEC enhancement can be observed in both predicted TEC maps and the CAS ones. Besides, the ionospheric TEC maps during 1–10 November 2021 were simulated by the bi-LSTM model, and the results are shown in Video 1. Video 1 shows that the bi-LSTM model captures the sudden ionospheric perturbations during 6:00–17:00 UT on 4 November (the Dst value reached −105 nT at 13:00UT), which indicates that the bi-LSTM model has the capability of predicting ionospheric responses to severe space weather. The third column of Figure 11 shows that the difference is slightly larger under the strong geomagnetic storm conditions and most within 2.5 TECU at 5:00 (Dst = −37 nT) and 23:00 (Dst = −38) UT and 6.2 TECU at 11:00 (Dst = −86 nT) and 17:00 (Dst = −68 nT) UT. Furthermore, 10 randomly selected minor to

moderate geomagnetic storms were also used for analysis, and the results show that the differences are primarily within 1.5 TECU at 5:00 and 11:00 UT and 2.5 TECU at 17:00 and 23:00 UT. These results suggest that the new model performs well for TEC predictions under geomagnetic storm conditions. However, the prediction accuracy under geomagnetic storm conditions is worse than that under geomagnetic quiet conditions, especially in low latitude regions. The lower accuracy in low latitude regions is probably due to the complexity of the ionospheric structure over low latitudes, such as the equatorial ionization anomaly (EIA) (Song et al., 2018; Xiong et al., 2021). Besides, according to Li, Wang, et al. (2021), the performance of the CAS GIMs is poor in low-latitude regions from both Jason VTEC and GPS dSTEC analyses. This may affect the quality of the evaluation of the new model over low latitude regions. In addition, the poor prediction accuracy of the new model under geomagnetic storm conditions may be associated with insufficient observations. This is because, compared with a large number of measurements under geomagnetic quiet conditions, some of the observations under geomagnetic storm conditions are likely to be regarded as "noise" values in the training process. As a result, separate modeling of the ionospheric TEC under geomagnetic quiet and storm conditions is necessary for improving the prediction ability under geomagnetic storm conditions.

5. Discussion and Conclusion

A new regional ionospheric TEC prediction model was developed over China region using the bi-LSTM method and long-term observations from 257 ground-based GPS stations in the CMONOC in the period from January 2018 to December 2021. The performance of the bi-LSTM model was evaluated using test data set (from June 2021 to December 2021) and observations at 12 stations evenly distributed throughout China. The accuracy of the bi-LSTM model was also compared with the IRI-2016, ANN, and LSTM models. Results showed that the bi-LSTM model outperforms all the other three models, in terms of correlation coefficients and RMSEs. Furthermore, the bi-LSTM model was evaluated for different geographical locations, different local times, different seasons, and different geomagnetic activity conditions at the 12 test stations. It was found that the diurnal variation, seasonal variation, and variations under geomagnetic storm conditions are well captured by the bi-LSTM model. In addition, the bi-LSTM model performs well during nighttime at higher latitude stations, and the TEC maps predicted from the bi-LSTM model show good agreement with the CAS TEC maps.

The GPS observational data used in the development of the bi-LSTM model are from a period of low solar activity, and the mean of the F10.7 index during the period is under 75. Thus, the new model may not perform well under high solar activity conditions. Srivani et al. (2019) used data during the descending phase (2009–2011) as training data and tested the performance of the LSTM model during the ascending phase (2012). The results showed that the RMSE of the LSTM model at the Bengaluru station (16.26°N, 80.44°E) was larger than that of the LSTM model, which trained with the VTEC values during the ascending phase (2009–2015) and tested during the descending phase (2016). Moreover, Srivani et al. (2019) and Ruwali et al. (2021) stated that the RMSE increased as the size of the training data set decreased. Hence more extended periods of data, particularly from high solar activity periods, may be worth testing for the improvement of the prediction accuracy of the bi-LSTM model.

Furthermore, the bi-LSTM model shows good performance for short-term TEC prediction, and the longer the time for the prediction, the poorer the performance is. Liu et al. (2020) used the LSTM method to predict the 256 spherical harmonic coefficients to construct GIMs. Evaluation results of the GIMs showed that the RMSE of the first/second hour ahead predictions was 1.27/2.20 TECU during geomagnetic storm conditions and 0.86/1.51 TECU during geomagnetic quiet conditions. Ruwali et al. (2021) used a hybrid model, which combined the LSTM with a convolution neural network (CNN), to predict the ionospheric TEC for a low-latitude GNSS station. The findings were that as the number of hours for prediction increased, the RMSE increased, and the RMSEs of the 1, 2, 3, 4, and 5 hr ahead predictions were 2.247, 3.73, 4.429, 4.813, and >4.85 TECU, respectively. Xiong et al. (2021) proposed a novel extended encoder-decoder long short-term memory neural network (ED-LSTME) to predict 3 hr ahead TEC using 1-day historical input TEC data. Results of the model established for station HRBN showed that the RMSE of the ED-LSTME model was 1.455 TECU, which is obviously larger than the RMSEs of the bi-LSTM model for the 1 hr (0.743 TECU) and 2 hr (0.998 TECU) ahead predictions tested in this study. Zewdie et al. (2021) applied an LSTM method to predict the TEC at an equatorial GPS station up to 5 hr ahead, with a 30-min interval, and results indicated that the correlation coefficient decreased while the RMSE increased as the time of the prediction is further into the future. Moreover, Chen et al. (2022) used four different

LSTM-based algorithms (single-step self-prediction model, single-step auxiliary prediction model, multi-step self-prediction model, and multi-step auxiliary prediction [MSAP] model) to predict global IGS-TEC maps. They found that the MSAP model can effectively alleviate the increasing error with prediction time; the MSAP model can better predict the global IGS-TEC in the next 6 days with RMSE of 3.511 TECU, which is much smaller than 5.593 TECU of the IRI-2016 model. Therefore, long-term prediction of the ionospheric TEC with high accuracy will be investigated in our further studies.

Finally, the new model captures the variations of the ionosphere TEC under geomagnetic storm conditions. However, the prediction capability of the new model under geomagnetic storm conditions is worse than that under geomagnetic quiet conditions. It is suggested that separately modeling the ionospheric TEC under geomagnetic storm conditions may improve the model performance under geomagnetic storm conditions, which will be investigated in our future work.

Data Availability Statement

We are very grateful to the providers of all the data used in this work for making their data available. The ground-based GPS data are available from the Crustal Movement Observation Network of China (CMONOC) (http://www.shao.ac.cn/shao_gnss_ac). The solar activity index F10.7 data are available from the Goddard Space Flight Center (https://omniweb.gsfc.nasa.gov/). The geomagnetic activity index Dst data are available from the World Data Center for Geomagnetism, Kyoto (http://wdc.kugi.kyoto-u.ac.jp/). The global ionospheric maps are available from the Chinese Academy of Sciences (ftp://ftp.gipp.org.cn/).

References

Badeke, R., Borries, C., Hoque, M. M., & Minkwitz, D. (2018). Empirical forecast of quiet time ionospheric Total Electron Content maps over Europe. *Advances in Space Research*, *61*(12), 2881–2890. https://doi.org/10.1016/j.asr.2018.04.010

Bailey, G. J., Balan, N., & Su, Y. Z. (1997). The Sheffield University plasmasphere ionosphere model—A review. *Journal of Atmospheric and Solar-Terrestrial Physics*, *59*(13), 1541–1552. https://doi.org/10.1016/S1364-6826(96)00155-1

Bengio, Y., Simard, P., & Frasconi, P. (1994). Learning long-term dependencies with gradient descent is difficult. *IEEE Transactions on Neural Networks*, *5*(2), 157–166. https://doi.org/10.1109/72.279181

Bent, R. B., Llewellyn, S. K., & Walloch, M. K. (1972). *Description and evaluation of the Bent ionospheric model*. DBA Systems.

Bilitza, D. (1990). International reference ionosphere 1990. *Planetary and Space Science*, *10*(4), 544. https://doi.org/10.1016/0032-0633(92)90174-M

Bilitza, D. (2018). IRI the international standard for the ionosphere. *Advances in Radio Science*, *16*, 1–11. https://doi.org/10.5194/ars-16-1-2018

Bilitza, D., Altadill, D., Truhlik, V., Shubin, V., Galkin, I., Reinisch, B., & Huang, X. (2017). International Reference Ionosphere 2016: From ionospheric climate to real-time weather predictions. *Space Weather*, *15*(2), 418–429. https://doi.org/10.1002/2016SW001593

Cesaroni, C., Spogli, L., Aragon-Angel, A., Fiocca, M., Dear, V., De Franceschi, G., & Romano, V. (2020). Neural network based model for global Total Electron Content forecasting. *Journal of Space Weather and Space Climate*, *10*(11), 1–18. https://doi.org/10.1051/swsc/2020013

Chen, P., Yao, Y., & Yao, W. (2017). Global ionosphere maps based on GNSS, satellite altimetry, radio occultation and DORIS. *GPS Solutions*, *21*(2), 639–650. https://doi.org/10.1007/s10291-016-0554-9

Chen, Z., Jin, M., Deng, Y., Wang, J. S., Huang, H., Deng, X., & Huang, C. M. (2019). Improvement of a deep learning algorithm for total electron content maps: Image completion. *Journal of Geophysical Research: Space Physics*, *124*(1), 790–800. https://doi.org/10.1029/2018ja026167

Chen, Z., Liao, W., Li, H., Wang, J., Deng, X., & Hong, S. (2022). Prediction of global ionospheric TEC based on deep learning. *Space Weather*, *20*(4), e2021SW002854. https://doi.org/10.1029/2021sw002854

Cherniak, I., & Zakharenkova, I. (2018). Ionospheric total electron content response to the great American solar eclipse of 21 August 2017. *Geophysical Research Letters*, *45*(3), 1199–1208. https://doi.org/10.1002/2017gl075989

Elmunim, N. A., Abdullah, M., Hasbi, A. M., & Bahari, S. A. (2017). Comparison of GPS TEC variations with Holt-Winter method and IRI-2012 over Langkawi, Malaysia. *Advances in Space Research*, *60*(2), 276–285. https://doi.org/10.1016/j.asr.2016.07.025

Fuller-Rowell, T. J., & Rees, D. (1980). A three-dimensional time-dependent global model of the thermosphere. *Journal of the Atmospheric Sciences*, *37*(11), 2545–2567. https://doi.org/10.1175/1520-0469(1980)037<2545:Atdtdg>2.0.Co;2

Gallagher, D. L., Craven, P. D., & Comfort, R. H. (2000). Global core plasma model. *Journal of Geophysical Research*, *105*(A8), 18819–18833. https://doi.org/10.1029/1999JA000241

García-Rigo, A., Monte, E., Hernández-Pajares, M., Juan, J. M., Sanz, J., Aragón-Angel, A., & Salazar, D. (2011). Global prediction of the vertical total electron content of the ionosphere based on GPS data. *Radio Science*, *46*(6), RS0D25. https://doi.org/10.1029/2010RS004643

Giovanni, G. D., & Radicella, S. M. (1990). An analytical model of the electron density profile in the ionosphere. *Advances in Space Research*, *10*(11), 27–30. https://doi.org/10.1016/0273-1177(90)90301-F

Huang, Z., Li, Q. B., & Yuan, H. (2015). Forecasting of ionospheric vertical TEC 1-h ahead using a genetic algorithm and neural network. *Advances in Space Research*, *55*(7), 1775–1783. https://doi.org/10.1016/j.asr.2015.01.026

Huang, Z., & Yuan, H. (2014). Ionospheric single-station TEC short-term forecast using RBF neural network. *Radio Science*, *49*(4), 283–292. https://doi.org/10.1002/2013rs005247

Jakowski, N., Hoque, M. M., & Mayer, C. (2011). A new global TEC model for estimating transionospheric radio wave propagation errors. *Journal of Geodesy*, *85*(12), 965–974. https://doi.org/10.1007/s00190-011-0455-1

Kaselimi, M., Voulodimos, A., Doulamis, N., Doulamis, A., & Delikaraoglou, D. (2020). A causal long short-term memory sequence to sequence model for TEC prediction using GNSS observations. *Remote Sensing*, *12*(9), 1354. https://doi.org/10.3390/rs12091354

Ketkar, N. (2017). *Deep learning with Python: A hands-on introduction*. Apress. https://doi.org/10.1007/978-1-4842-2766-4

Klobuchar, J. A. (1987). Ionospheric time-delay algorithm for single-frequency GPS users. *IEEE Transactions on Aerospace and Electronic Systems*, *23*(3), 325–331. https://doi.org/10.1109/TAES.1987.310829

Krankowski, A., Kosek, W., Baran, L. W., & Popinski, W. (2005). Wavelet analysis and forecasting of VTEC obtained with GPS observations over European latitudes. *Journal of Atmospheric and Terrestrial Physics*, *67*(12), 1147–1156. https://doi.org/10.1016/j.jastp.2005.03.004

Li, W., He, C., Hu, A., Zhao, D., Shen, Y., & Zhang, K. (2021). A new method for improving the performance of an ionospheric model developed by multi-instrument measurements based on artificial neural network. *Advances in Space Research*, *67*(1), 20–34. https://doi.org/10.1016/j.asr.2020.07.032

Li, W., Zhao, D., He, C., Shen, Y., Hu, A., & Zhang, K. (2021). Application of a multi-layer artificial neural network in a 3-D global electron density model using the long-term observations of COSMIC, Fengyun-3C, and Digisonde. *Space Weather*, *19*(3), 1–19. https://doi.org/10.1029/2020sw002605

Li, W., Zhao, D., Shen, Y., & Zhang, K. (2020). Modeling Australian TEC maps using long-term observations of Australian regional GPS network by artificial neural network-aided spherical cap harmonic analysis approach. *Remote Sensing*, *12*(23), 3851–3870. https://doi.org/10.3390/rs12233851

Li, Z., Wang, N., Liu, A., Yuan, Y., Wang, L., Hernández-Pajares, M., et al. (2021). Status of CAS global ionospheric maps after the maximum of solar cycle 24. *Satellite Navigation*, *2*(19), 1–15. https://doi.org/10.1186/s43020-021-00050-2

Li, Z., Yuan, Y., Li, H., Ou, J., & Huo, X. (2012). Two-step method for the determination of the differential code biases of COMPASS satellites. *Journal of Geodesy*, *86*(11), 1059–1076. https://doi.org/10.1007/s00190-012-0565-4

Li, Z., Yuan, Y., Wang, N., Hernandez-Pajares, M., & Huo, X. (2015). SHPTS: Towards a new method for generating precise global ionospheric TEC map based on spherical harmonic and generalized trigonometric series functions. *Journal of Geodesy*, *89*(4), 331–345. https://doi.org/10.1007/s00190-014-0778-9

Liu, A., Wang, N., Li, Z., Zhou, K., & Yuan, H. (2018). Validation of CAS's final global ionospheric maps during different geomagnetic activities from 2015 to 2017. *Results in Physics*, *10*, 481–486. https://doi.org/10.1016/j.rinp.2018.06.057

Liu, L., Zou, S., Yao, Y., & Wang, Z. (2020). Forecasting global ionospheric TEC using deep learning approach. *Space Weather*, *18*(11), 1–12. https://doi.org/10.1029/2020sw002501

Mannucci, A. J., Wilson, B. D., Yuan, D. N., Ho, C. H., Lindqwister, U. J., & Runge, T. F. (1998). A global mapping technique for GPS-derived ionospheric total electron content measurements. *Radio Science*, *33*(3), 565–582. https://doi.org/10.1029/97rs02707

Nava, B., Coïsson, P., & Radicella, S. M. (2008). A new version of the NeQuick ionosphere electron density model. *Journal of Atmospheric and Solar-Terrestrial Physics*, *70*(15), 1856–1862. https://doi.org/10.1016/j.jastp.2008.01.015

Ngwira, C. M., McKinnell, L.-A., Cilliers, P. J., & Coster, A. J. (2012). Ionospheric observations during the geomagnetic storm events on 24–27 July 2004: Long-duration positive storm effects. *Journal of Geophysical Research*, *117*(A9). https://doi.org/10.1029/2011ja016990

Okoh, D., Habarulema, J. B., Rabiu, B., Seemala, G., Wisdom, J. B., Olwendo, J., et al. (2020). Storm-time modeling of the African regional ionospheric total electron content using artificial neural networks. *Space Weather*, *18*(9), 1–16. https://doi.org/10.1029/2020SW002525

Okoh, D., Owolabi, O., Ekechukwu, C., Folarin, O., Arhiwo, G., Agbo, J., et al. (2016). A regional GNSS-VTEC model over Nigeria using neural networks: A novel approach. *Geodesy and Geodynamics*, *7*(1), 19–31. https://doi.org/10.1016/j.geog.2016.03.003

Okoh, D., Seemala, G., Rabiu, B., Habarulema, J. B., Jin, S., Shiokawa, K., et al. (2019). A neural network-based ionospheric model over Africa from constellation observing system for meteorology, ionosphere, and climate and ground global positioning system observations. *Journal of Geophysical Research: Space Physics*, *124*(12), 10512–10532. https://doi.org/10.1029/2019JA027065

Orus Perez, R. (2019). Using TensorFlow-based Neural Network to estimate GNSS single frequency ionospheric delay (IONONet). *Advances in Space Research*, *63*(5), 1607–1618. https://doi.org/10.1016/j.asr.2018.11.011

Pascanu, R., Mikolov, T., & Bengio, Y. (2013). *On the difficulty of training recurrent neural networks*. arXiv:1211.5063. Retrieved from https://arxiv.org/pdf/1211.5063.pdf

Razin, M. R. G., Voosoghi, B., & Mohammadzadeh, A. (2015). Efficiency of artificial neural networks in map of total electron content over Iran. *Acta Geodaetica et Geophysica*, *51*(3), 541–555. https://doi.org/10.1007/s40328-015-0143-3

Ren, X., Chen, J., Li, X., Zhang, X., & Freeshah, M. (2019). Performance evaluation of real-time global ionospheric maps provided by different IGS analysis centers. *GPS Solutions*, *23*(4), 1–17. https://doi.org/10.1007/s10291-019-0904-5

Rich, F. J., Sultan, P. J., & Burke, W. J. (2003). The 27-day variations of plasma densities and temperatures in the topside ionosphere. *Journal of Geophysical Research*, *108*(A7), 1297–1305. https://doi.org/10.1029/2002JA009731

Ruder, S. (2016). *An overview of gradient descent optimization algorithms*. arXiv:1609.04747. Retrieved from https://arxiv.org/pdf/1609.04747.pdf

Ruwali, A., Kumar, A. J. S., Prakash, K. B., Sivavaraprasad, G., & Ratnam, D. V. (2021). Implementation of hybrid deep learning model (LSTM-CNN) for ionospheric TEC forecasting using GPS data. *IEEE Geoscience and Remote Sensing Letters*, *18*(6), 1004–1008. https://doi.org/10.1109/lgrs.2020.2992633

Sabzehee, F., Farzaneh, S., Sharifi, M. A., & Akhoondzadeh, M. (2018). TEC regional modeling and prediction using ANN method and single frequency receiver over IRAN. *Annals of Geophysics*, *61*(1), 1–18. https://doi.org/10.4401/ag-7297

Schaer, S. (1999). *Mapping and predicting the earth's ionosphere using the Global Positioning System, (Doctoral dissertation)*. Bern University.

Sojka, J. J. (1989). Global scale, physical models of the *F* region ionospere. *Reviews of Geophysics*, *27*(3), 371–403. https://doi.org/10.1029/RG027i003p00371

Song, R., Zhang, X., Zhou, C., Liu, J., & He, J. (2018). Predicting TEC in China based on the neural networks optimized by genetic algorithm. *Advances in Space Research*, *62*(4), 745–759. https://doi.org/10.1016/j.asr.2018.03.043

Srivani, I., Siva Vara Prasad, G., & Venkata Ratnam, D. (2019). A deep learning-based approach to forecast ionospheric delays for GPS signals. *IEEE Geoscience and Remote Sensing Letters*, *16*(8), 1180–1184. https://doi.org/10.1109/lgrs.2019.2895112

Tebabal, A., Radicella, S. M., Damtie, B., Migoya-Orue', Y., Nigussie, M., & Nava, B. (2019). Feed forward neural network based ionospheric model for the East African region. *Journal of Atmospheric and Solar-Terrestrial Physics*, *191*, 105052–105061. https://doi.org/10.1016/j.jastp.2019.05.016

Thomas, J. N., Huard, J., & Masci, F. (2017). A statistical study of global ionospheric map total electron content changes prior to occurrences of $M \geq 6.0$ earthquakes during 2000–2014. *Journal of Geophysical Research: Space Physics*, *122*(2), 2151–2161. https://doi.org/10.1002/2016ja023652

Tulasi Ram, S., Sai Gowtam, V., Mitra, A., & Reinisch, B. (2018). The improved two-dimensional artificial neural network-based ionospheric model (ANNIM). *Journal of Geophysical Research: Space Physics*, *123*(7), 5807–5820. https://doi.org/10.1029/2018ja025559

Uwamahoro, J. C., Giday, N. M., Habarulema, J. B., Katamzi-Joseph, Z. T., & Seemala, G. K. (2018). Reconstruction of storm-time total electron content using ionospheric tomography and artificial neural networks: A comparative study over the African region. *Radio Science*, *53*(11), 1328–1345. https://doi.org/10.1029/2017rs006499

Wang, N., Yuan, Y., Li, Z., & Huo, X. (2016). Improvement of Klobuchar model for GNSS single-frequency ionospheric delay corrections. *Advances in Space Research*, *57*(7), 1555–1569. https://doi.org/10.1016/j.asr.2016.01.010

Williscroft, L.-A., & Poole, A. W. V. (1996). Neural networks, foF2, sunspot number and magnetic activity. *Geophysical Research Letters*, *23*(24), 3659–3662. https://doi.org/10.1029/96GL03472

Xiong, P., Zhai, D., Long, C., Zhou, H., Zhang, X., & Shen, X. (2021). Long short-term memory neural network for ionospheric total electron content forecasting over China. *Space Weather*, *19*(4), 1–20. https://doi.org/10.1029/2020sw002706

Zewdie, G. K., Valladares, C., Cohen, M. B., Lary, D. J., Ramani, D., & Tsidu, G. M. (2021). Data-driven forecasting of low-latitude ionospheric total electron content using the random forest and LSTM machine learning methods. *Space Weather*, *19*(6), 1–11. https://doi.org/10.1029/2020sw002639

Zhukov, A. V., Yasyukevich, Y. V., & Bykov, A. E. (2020). GIMLi: Global Ionospheric total electron content model based on machine learning. *GPS Solutions*, *25*(19), 1–9. https://doi.org/10.1007/s10291-020-01055-1